SCIENCE CHINA
Information Sciences

• RESEARCH PAPER •

August 2023, Vol. 66 182405:1–182405:9
https://doi.org/10.1007/s11432-022-3694-4

Boosted high-temperature electrical characteristics of AlGaN/GaN HEMTs with rationally designed compositionally graded AlGaN back barriers

Haochen ZHANG[†], Yue SUN[†], Kunpeng HU, Lei YANG, Kun LIANG, Zhanyong XING, Hu WANG, Mingshuo ZHANG, Huabin YU, Shi FANG, Yang KANG & Haiding SUN[*]

School of Microelectronics, University of Science and Technology of China, Hefei 230026*, China*

Received 24 September 2022/Revised 7 December 2022/Accepted 31 January 2023/Published online 26 July 2023

Abstract Wide bandgap GaN-based HEMTs have shown great potential as key components in various power electronic systems but still face challenges in the pursuit of devices with stable operation capability especially in harsh environments. Here, we report a high-performance double heterojunction (DH) based AlGaN/GaN HEMT by incorporating a decreasing-Al-composition (DAC) graded AlGaN back barrier (BB) beneath the GaN channel. Thanks to the improved electron confinement enabled by graded BB, the DH-HEMT exhibits significantly improved on-state drain current density and off-state breakdown voltage compared with a single heterojunction (SH) based HEMT. More intriguingly, with an additional SiN_x passivation layer, the surface states of the DH-HEMTs can be effectively suppressed, leading to an almost constant off-state leakage current and negligible gate contact degradation across the temperature range from 25°C to 150°C. These results highlight the superiority and reliability of the proposed graded AlGaN BB to boost device characteristics for applications under high temperatures and harsh conditions.

Keywords AlGaN/GaN HEMT, graded AlGaN back barrier, SiN_x passivation, DHHEMT, high temperature stability

Citation Zhang H C, Sun Y, Hu K P, et al. Boosted high-temperature electrical characteristics of AlGaN/GaN HEMTs with rationally designed compositionally graded AlGaN back barriers. Sci China Inf Sci, 2023, 66(8): 182405, https://doi.org/10.1007/s11432-022-3694-4

1 Introduction

Wide bandgap semiconductor Al(Ga)N alloys possess superior intrinsic properties, such as large breakdown electric field, high electron mobility, and decent thermal conductivity [1–3]. Particularly, by taking advantage of the polarization effects of III-nitrides, we can construct AlGaN/GaN-based heterojunction field-effect transistors (HFETs), also well-known as high-electron-mobility transistors (HEMTs), with high-concentration two-dimensional electron gases (2DEGs) as conductive channels [4–6]. These material properties have fundamentally established AlGaN/GaN HEMTs as one of the most promising technologies for next-generation power electronics systems with compact sizes, higher power efficiency, and faster switching speed to achieve a carbon-neutral future [7–9]. Currently, AlGaN/GaN HEMTs have achieved preliminary implementations in the fields such as consumer electronics and wireless communication. For the benefit of mass production, the mainstream HEMT structure is simply based on a single heterojunction (SH) incorporating a GaN channel and an AlGaN barrier, whose Al composition, doping concentration, and layer thickness are relatively fixed. However, further device optimizations, such as band engineering and channel modulation of such SH-HEMTs, are largely limited. To continuously propel the development of GaN HEMT technologies, researchers have put forward multiple strategies to tailor the simple AlGaN/GaN SH and exploit the device characteristics toward targeted applications [1,10–12].

* Corresponding author (email: haiding@ustc.edu.cn)
† Zhang H C and Sun Y have the same contribution to this work.

One of the popular approaches for SH optimization is to insert a back barrier (BB) layer beneath the GaN channel and construct a double heterojunction (DH) HEMT. In principle, the BB is designed to lift the band structure beneath the 2DEG channel and thereby realize better carrier confinement under high-voltage or high-frequency operation [13,14]. Recently, a DH-HEMT incorporating BBs with different layer thicknesses [15], various group-III elements (B, Al, Ga, and In) [16–18], and special profiles of alloy compositions [19,20], have been proposed and intensively investigated. Among various BB structures, one particular design scheme is to adopt a decreasing-Al-composition (DAC) graded AlGaN BB layer along the growth direction to build a DH-HEMT. Numerical studies have confirmed that such graded BBs can suppress electron concentration in the buffer layer by avoiding forming parasitic channels [20–22]. Besides, it has been reported that the DAC graded BBs can tune the internal strain in the epilayers [23]. However, the impacts of DAC graded AlGaN BB on the high-temperature electrical performance of HEMTs, together with the additional device-level optimizations, for example, by introducing a surface passivation layer to improve the device stability, still require experimental explorations and verification.

In this work, we comprehensively investigated and evaluated the device characteristics of the DH-HEMT with a DAC graded AlGaN BB and compare these results with the SH-HEMT by operating them over a wide temperature range from 25°C to 150°C. It is found that the DH-HEMT can outperform SH-HEMT significantly by possessing higher on-state drain current density (J_D), a larger off-state breakdown voltage (V_{BD}), and effectively suppressed current dispersion under high temperature, confirming the advantages of the improved carrier confinement facilitated by the DAC graded BB. Furthermore, with an additional SiN_x passivation layer, the on-state J_D and off-state V_{BD} of devices can be further enhanced. More importantly, we found that the BB-improved carrier confinement and SiN_x-suppressed surface states can mutually improve the device stability operating under high temperature, featuring a nearly negligible temperature-induced off-state leakage current dispersion, suppressed Schottky gate contact inhomogeneity, and complete elimination of gate degradation under the high-temperature operation of the DH-HEMT. These results highlight that the proposed DH-HEMT with a properly designed DAC graded BB and an additional SiN_x passivation layer can significantly improve device stability under harsh environments.

2 Material characterization and device fabrication

Figures 1(a) and (b) show the schematic illustration of the two devices, i.e., SH- and DH-HEMT, investigated in this study. Both devices were grown by metal-organic chemical vapor deposition (MOCVD) on the 2-inch flat sapphire substrate (FSS) with a 100-nm-thick physical vapor deposited (PVD) AlN nucleation layer. The epitaxial structure of the SH-HEMT consists of a 5 μm GaN buffer layer, a 1.7 μm unintentionally doped GaN buffer layer, a 300 nm GaN channel layer, a 1 nm AlN spacer layer, a 20 nm $\mathrm{Al}_{0.25}\mathrm{Ga}_{0.75}\mathrm{N}$ barrier layer, and a 2 nm GaN cap layer. As for the DH-HEMT, a 1 μm BB with a decreasingly graded Al composition from 0.2 to 0 was inserted between the GaN buffer and 100 nm GaN channel, as shown in Figure 1(b). To epitaxially grow the DAC graded AlGaN BB, we initially injected sufficient Al flux (Trimethylaluminum, TMAl) to grow AlGaN alloy with 20% Al content based on our growth calibration. Thereby, we slowly decreased the Al flux to zero while simultaneously increasing the Ga flux (Trimethylgallium, TMGa) with a linearly increased flow rate to obtain a decreasingly graded Al composition profile. This Al grading scheme was intended to realize energy band lifting under the 2DEG channel and avoid the formation of a parasitic p-type conductive channel [20]. Figure 1(c) shows the electron density (N_D) extracted from 100 kHz C-V measurements for both SH- and DH-HEMT. It can be found that DH-HEMT has a steeper decrease at the AlGaN/GaN heterointerface and reduced electron density at the buffer region compared with SH-HEMT, verifying the functionality of the DAC graded AlGaN BB.

Then, we characterized the material properties of the as-grown SH- and DH-HEMT by X-ray diffraction (XRD) analysis. Figures 2(a) and (b) present the (102) and (002) rocking curves of both samples, respectively. It can be found that although the values of the (102) FWHM (full width half maximum) for both samples are similar, a higher (002) FWHM value is observed in DH-HEMT, indicating that the screw-type threading dislocation, which normally acts as the leakage path in GaN-based devices [24,25], is higher in the DH-HEMT than that in the SH-HEMT. The corresponding impacts on the electrical performance of the two devices will be discussed later. Figure 2(c) further compares the high-resolution XRD results of both SH- and DH-HEMT. Obviously, the DH-HEMT has multiple low-Al-composition

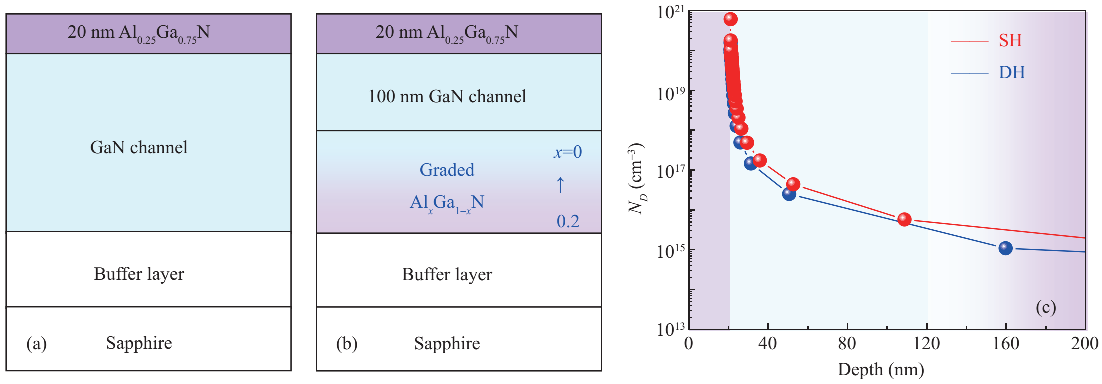

Figure 1 (Color online) (a) and (b) depict the epitaxial structures of SH- and DH-HEMT, respectively (not in scale). The GaN cap and AlN spacer are not displayed. (c) shows the extracted electron concentration (N_D) of the two devices from C-V measurements.

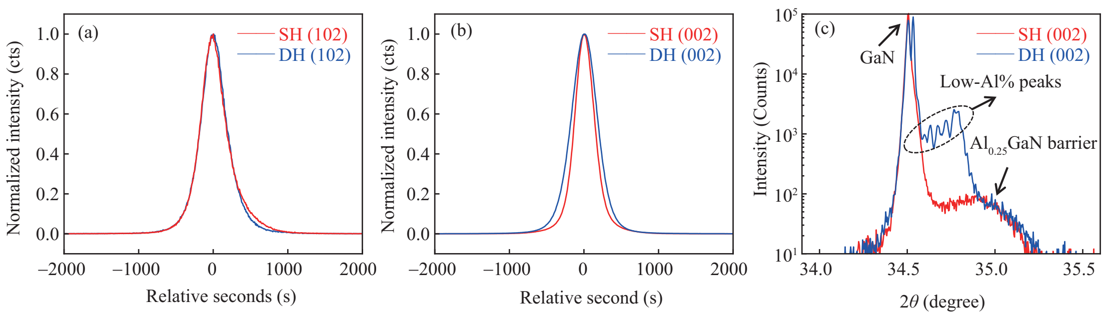

Figure 2 (Color online) (a) and (b) show the (102) and (002) rocking curves of SH- and DH-HEMT. (c) demonstrates the (002) high-resolution XRD results of SH- and DH-HEMT, revealing the existence of low-Al% peaks of the DAC graded AlGaN BB.

peaks between the main peak (GaN) and the labeled peak ($Al_{0.25}Ga_{0.75}N$ barrier layer), indicating the existence of the DAC graded AlGaN BB.

The device fabrication process started with rinsing in organic solvents before Cl_2-based inductively coupled plasma (ICP) etching for mesa definition. The etching depth was 200 nm to fully separate any possible conductive channel at the AlGaN/GaN or GaN/BB interface for better device isolation. Then, the wafer was treated with a 25% tetramethylammonium hydroxide (TMAH) solution to remove sidewall etching damage. The metallization schemes of the Ohmic contacts for the source/drain electrodes and the Schottky contact for the gate electrode were set as Ti/Al/Ni/Au (20/100/40/50 nm) and Ni/Au (20/100 nm), respectively. The devices under test (DUTs) feature the same device dimensions of gate width (W_G) of 50 μm, gate length (L_G) of 3 μm, and source-drain spacing ($L_{\rm SD}$) of 10 μm. For the passivated devices, 200-nm-thick SiN_x was deposited on the device surface by plasma-enhanced chemical vapor deposition (PECVD) at 350°C and 1000 Torr chamber pressure. The gases and flow rate for SiN_x deposition were set as 5%SiH_4/N_2 (30 sccm), NH_3 (45 sccm), and N_2 (1000 sccm).

3 Results and discussions

3.1 Room-temperature DC characteristics of SH- and DH-HEMTs

Figure 3 compares the room-temperature direct current (DC) electrical characteristics of both SH- and DH-HEMT with or without SiN_x passivation. At the on-state, it is found that the drain current density (J_D) of the unpassivated DH-HEMT is higher than that of SH-HEMT, as compared in both transfer curves (Figure 3(a)) and output curves (Figure 3(b)), verifying stronger carrier confinement in the DH-HEMT enabled by the graded AlGaN BB. Furthermore, the additional SiN_x passivation layer can boost the on-state device performance of both devices, featuring increased maximum output J_D and reduced on-resistance ($R_{\rm ON}$), as shown in Figure 3(b). These improvements should be attributed to the external tensile strain, as well as passivation effects on the net polarization charges on the device surface, facilitated

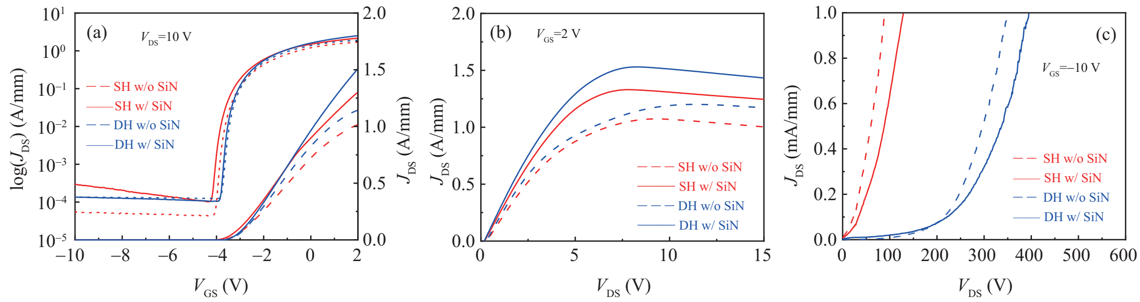

Figure 3 (Color online) DC characteristics of SH- and DH-HEMT with or without SiN_x passivation. (a) Transfer curves at V_{DS} = 10 V in linear and semi-log scales; (b) output curves at V_{GS} = 2 V; (c) V_{BD} measured under V_{GS} = −10 V.

by the introduction of the SiN_x layer, which can further increase the 2DEG concentration [26]. For the off-state device performance, the transfer curves in Figure 3(a) reveal that the unpassivated DH-HEMT (blue dot line) has a higher reverse drain leakage current ($J_{D,\text{off}}$) than the unpassivated SH-HEMT (red dot line). However, after the device passivation, the SH-HEMT exhibited an increased $J_{D,\text{off}}$ (red solid line), which can be attributed to the plasma damage during the PECVD process. Meanwhile, $J_{D,\text{off}}$ of the passivated DH-HEMT (blue solid line) was almost identical to that of the bare device with negligible degradation. Combining the BB-improved carrier confinement and SiN_x-suppressed surface states, the passivated DH-HEMT can achieve the highest off-state breakdown voltage (V_{BD}, defined as V_{DS} at J_{DS} = 1 mA/mm), as compared in Figure 3(c).

3.2 Effect of SiN_x passivation on HEMT characteristics

To comprehend the effect of SiN_x passivation on the device performance of the SH- and DH-HEMT, we further analyze the mechanisms from the perspective of the gate current (I_G) by decomposing it into three components, including:

(1) Thermal emission (TE), which is the dominant phenomenon in the forward bias range, as given by

$$J_{\text{TE}} = J_0 \left\{ \exp\left(\frac{qV}{\eta kT}\right) - 1 \right\} = A^* T^2 \exp\left(-\frac{q\Phi_B}{kT}\right) \left\{ \exp\left(\frac{qV}{\eta kT}\right) - 1 \right\}, \tag{1}$$

where A^* is the effective Richardson constant, T is the temperature, q is the electron charge, k is the Boltzmann constant, η is the ideal factor and Φ_B is the Schottky barrier height.

(2) Poole-Frenkel (PF) emission, which accounts for the main component of the reverse gate current, as given by

$$J_{\text{PF}} = CE \exp\left[-\frac{q\left(\Phi_t - \sqrt{(qE/\pi\varepsilon_i)}\right)}{kT} \right], \tag{2}$$

$$E = \frac{q(\sigma_b - n_s)}{\varepsilon}, \tag{3}$$

where C is a constant, Φ_t is the barrier height for the electron emission from the trap state, ε_i is the permittivity of the semiconductor at high frequency, σ_b is the bound charge at the hetero-interface, n_s is the 2DEG concentration at the hetero-interface and ε is the permittivity of the barrier.

(3) Trap-assisted tunneling (TAT) current flowing from the gate to the channel as given by

$$J_{\text{TAT}} = J_{02} \left\{ \exp\left(\frac{q(V - V_0)}{\eta_2 kT}\right) - 1 \right\}, \tag{4}$$

where J_{02}, V_0, and η_2 are the parameters used to fit the experimental characteristics near zero bias.

Figures 4(a) and (d) demonstrate the measured I_G-V_{GS} curves ($V_{DS} = 0$ V) of both DH- and SH-HEMT before and after SiN_x passivation. The experimental results were fitted with TAT, PF, and TE models. It can be found the unpassivated DH-HEMT exhibited a distinct "double-barrier" phenomenon at 0 V $< V_{GS} <$ 1 V due to the spatial inhomogeneity at the Schottky/semiconductor interface [27]. The fitting results shown in Figure 4(b) reveal that there existed a large component of TAT current at this V_{GS}

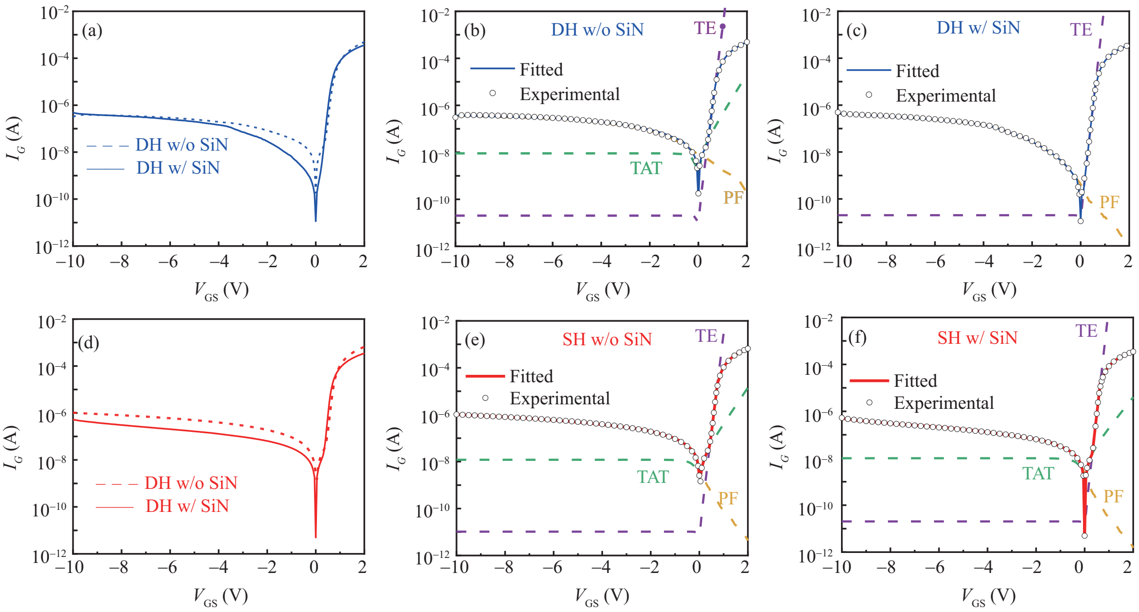

Figure 4 (Color online) (a) The experimental I_G-V_{GS} curves of DH-HEMT without/with passivation. Their fitting results by three current components are shown in (b) and (c), respectively. (d) The experimental I_G-V_{GS} curves of SH-HEMT without/with passivation. Their fitting results by three current components are shown in (e) and (f), respectively.

regime. With an additional SiN_x layer to passivate the surface states, the TAT current can be suppressed and this non-ideal behavior of Schottky contact was effectively eliminated, as confirmed by the fitting results in Figure 4(c). In contrast, the double-barrier effect observed in the SH-HEMT (Figure 4(d)) can hardly be improved by the passivation process, indicating that the TAT process is mainly caused by the buffer-induced defects [28] instead of surface states, and the SiN_x surface passivation process is ineffective in this case. The observed surface states evolution of SH- and DH-HEMT before and after passivation can be further confirmed by the extracted subthreshold swing (SS) values from Figure 3(a), which are mainly determined by the surface states [29–31]. For the unpassivated devices, DH-HEMT has a larger SS value of 105.45 mV/dec compared with SH-HEMT (SS = 94.28 mV/dec). After SiN_x passivation, the SS values of DH-HEMT can be reduced to 82.58 mV/dec, while that of SH-HEMT is only slightly changed to 90.64 mV/dec, conforming to the conclusion from the I_G-V_{GS} analysis.

Furthermore, to quantitatively evaluate the evolution of surface defect density and distribution of the SH- and DH-HEMT before and after passivation, we employed the frequency-dependent capacitance-voltage (C-V-f) measurements based on Mercury C-V platform (Material Development Corporation, MDC 802B). Thereafter, the parallel conductance (G_p/ω) under frequencies ranging from 1 kHz to 1 MHz was extracted and plotted in Figure 5(a1) (SH-HEMT w/o SiN_x), Figure 5(a2) (DH-HEMT w/o SiN_x), Figure 5(b1) (SH-HEMT w/ SiN_x), and Figure 5(b2) (DH-HEMT w/ SiN_x). The interface trap density (D_T), time constant (τ), and corresponding energy level (E_T) can be obtained by fitting the experimental G_p/ω-ω relationship, as given by [32]

$$\frac{G_p}{\omega} = \frac{qD_T}{2\omega\tau}\ln\left[1+(\omega\tau)^2\right], \tag{5}$$

$$\tau = \frac{1}{v_{\mathrm{th}}\sigma_n N_C}\exp\left(\frac{E_T}{kT}\right), \tag{6}$$

where q is the elementary charge; T is the Kelvin temperature; $N_C = 4.3\times10^{14}\times T^{3/2}$ cm^{-3} is the effective density of states in the conduction band in GaN, $v_{\mathrm{th}} = 2\times10^7$ cm/s is the average thermal velocity of electrons, and $\sigma_n = 1\times10^{-14}$ cm^2 is the capture cross section of the trap states. Figure 5(c) concludes the extracted interface state density and distribution of four devices. For the unpassivated devices, the density of relatively shallow surface defects is close, on the order of 10^{14} cm$^{-2}\cdot$ eV^{-1}, as labelled by red dots (SH-HEMT) and blue dots (DH-HEMT). After SiN_x passivation, the shallow traps of the DH-HEMT can be largely reduced (purple dots) and become lower than that of the passivated SH-HEMT (orange dots). It has been reported that TAT current and resulted in double barrier phenomenon

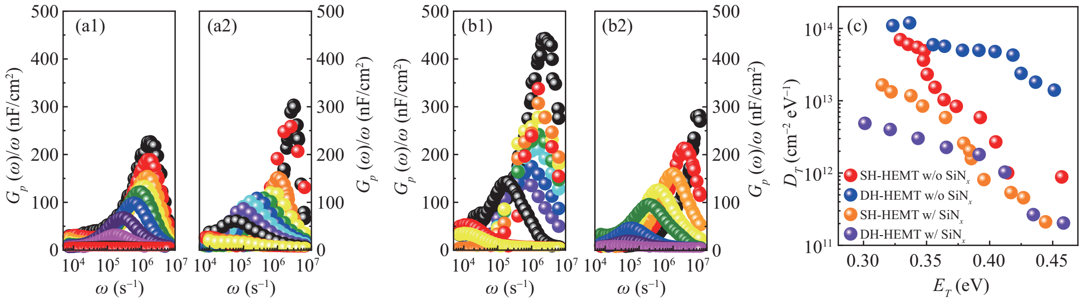

Figure 5 (Color online) Measured $C_p(\omega)/\omega$-ω relationship of (a1) SH-HEMT without SiN_x, (a2) DH-HEMT without SiN_x, (b1) SH-HEMT with SiN_x, and (b2) DH-HEMT with SiN_x. (c) extracted surface defect density and distribution from (a) and (b).

in I_G-V_{GS} curves are mainly caused by shallow trap states [33, 34], which agrees well with the observed evolution trend of the I_G behavior and fitted TAT current component of our investigated devices.

In addition, we further studied the PF current to analyze the reverse leakage current behavior of the devices. It can be found that the PF current of the SH-HEMT is reduced after SiN_x passivation, as shown in Figure 4(d). According to (2) and (3), a lower PF current can be attributed to the higher electron concentration (n_s) in the conductive channel, confirming the increased 2DEG concentration enabled by SiN_x layer. In contrast, the PF current of the DH-HEMT with SiN_x is only reduced at $V_{GS} > -4$ V region and is identical with that of the unpassivated device at the off-state ($V_{GS} < -4$ V), as shown in Figure 4(a). This behavior indicates that even though the equilibrium 2DEG concentration is increased in the passivated DH-HEMT, the inserted DAC graded AlGaN BB can confine the electrons under large reverse V_{GS} bias and prevent them from penetrating into the buffer region to form the parasitic leakage current path. As a result, the $J_{D,\mathrm{off}}$ degradation of the DH-HEMT is negligible while that of SH-HEMT can be obviously observed, as labelled by the red solid line and red dash line in Figure 3(a).

3.3 High-temperature characterizations of HEMTs

Furthermore, the carrier confinement capability of the graded AlGaN BB, as well as the surface passivation effects provided by the PECVD-SiN_x, were evaluated under high temperatures to demonstrate the device stability enabled by the rational device design. Figures 6(a) and (b) compare the temperature-dependent transfer curves of the unpassivated SH- and DH-HEMT. Both devices suffered from the on-state current drop at high temperatures, as shown in Figure 6(e), which should be attributed to the increased phonon scattering effects [35]. Interestingly, the deterioration of the off-state leakage current of the DH-HEMT was largely suppressed compared with that of SH-HEMT. The statistical comparisons are concluded in Figure 6(f), where distinct differences can be found between the SH-HEMT w/o SiN_x (red lines) and DH-HEMT w/o SiN_x (blue lines). The improvements revealed that the DAC graded AlGaN BB can provide sufficient carrier confinement under large reverse V_{GS} even at elevated temperatures. Furthermore, when the DH-HEMT is passivated with SiN_x, the temperature-induced $J_{D,\mathrm{off}}$ dispersion was almost eliminated within the temperatures from 25°C to 150°C, as shown in Figure 6(d) and the purple line in Figure 6(f). This superior property proves that the surface traps of the DH-HEMT can be well suppressed by a proper surface passivation scheme, and is unambiguously effective under high temperatures. In comparison, the passivated SH-HEMT still exhibits obvious $J_{D,\mathrm{off}}$ degradation at higher temperatures (Figure 6(c) and orange line in Figure 6(e)) even though SiN_x can suppress the surface traps, conforming to the discussions and conclusions in the previous sections.

Figures 7(a) and (b) further compare the temperature-dependent I_G-V_{GS} curves of the passivated SH and DH-HEMT. It can be found that SH-HEMT suffers from large gate current dispersion and undesired Schottky gate contact degradation at high temperatures. In contrast, the device with graded AlGaN BB exhibits an almost constant gate current and a completely suppressed "double-barrier" behavior under all the measured temperatures. Here, we further employed two-dimensional variable range hopping (2D-VRH) (7) [36,37] to characterize the gate current components after SiN_x passivation within the measured temperatures.

$$\sigma \propto \exp\left[-\left(\frac{1}{T}\right)^{\frac{1}{3}}\right], \tag{7}$$

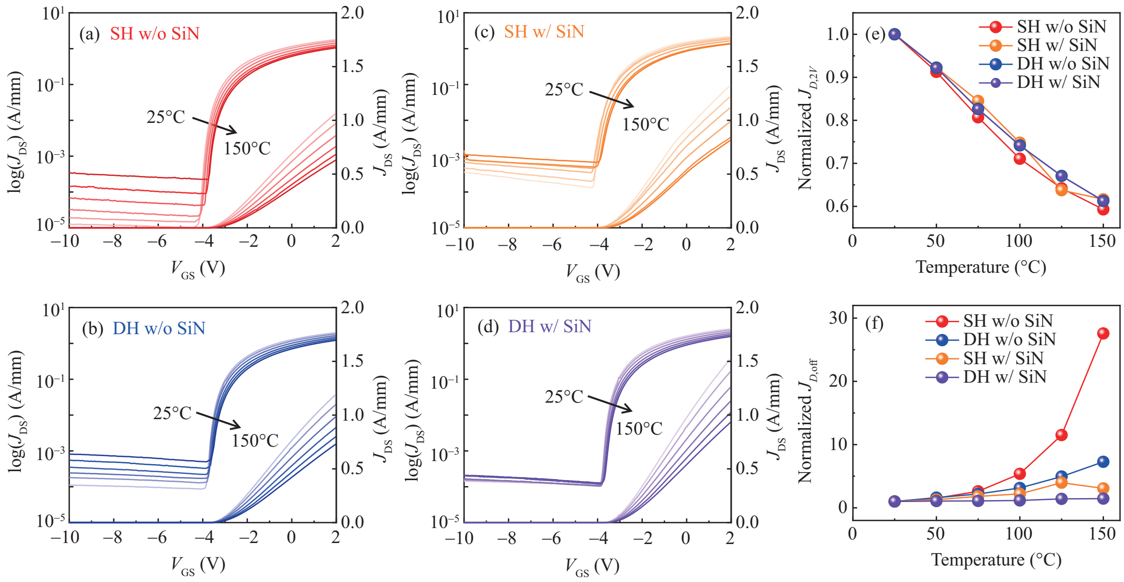

Figure 6 (Color online) Temperature-dependent transfer curves of the (a) unpassivated SH-HEMT, (b) unpassivated DH-HEMT, (c) passivated SH-HEMT, and (d) passivated DH-HEMT. (e) and (f) show the evolution of $J_{D,2V}$ and $J_{D,\mathrm{off}}$ of the SH- and DH-HEMT with/without SiN_x passivation along with operation temperatures.

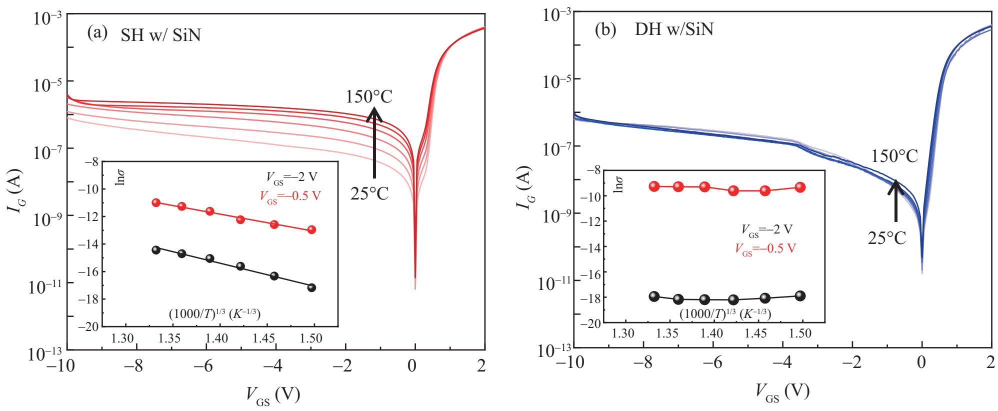

Figure 7 (Color online) Temperature-dependent I_G-V_{GS} curves of the passivated (a) SH-HEMT and (b) DH-HEMT. The insets demonstrate the extracted lnσ values within the measured temperatures characterizing the 2D-VRH transport process.

where σ is the conductance. The inset of Figures 7(a) and (b) demonstrate the evolution of lnσ at $V_{GS} = -2$ V (reverse region of TAT) and $V_{GS} = 0.5$ V (forward region of TAT) along with $1/T^{1/3}$ for the passivated SH- and DH-HEMT, respectively. It can be found that the lnσ values of the passivated SH-HEMT exhibit a linear correlation with $1/T^{1/3}$ from 25°C to 150°C, revealing that 2D-VRH is the main transport mechanism of I_G. In comparison, the lnσ of DH-HEMT is independent of the operating temperatures in both the reverse and forward regions, indicating that SiN_x passivation can effectively restrain the surface-hopping-induced gate leakage current of DH-HEMT with graded AlGaN BB.

4 Conclusion

In this study, a high-performance AlGaN/GaN-based DH-HEMT with superior device stability under high temperatures is demonstrated. With a rationally designed decreasing-Al-component graded AlGaN BB, the DH-HEMT can outperform its counterpart SH-HEMT featuring higher on-state current, larger off-state breakdown voltage, and smaller current degradation under high temperatures, thanks to the improved carrier confinement abilities provided by the BB. Additionally, with further surface passivation by PECVD-SiN_x, the high-temperature current dispersion and Schottky gate contact degradation can be almost eliminated within the temperature from 25°C to 150°C. These significantly improved device performance and high-temperature stability have highlighted the great potential of graded AlGaN BBs to tailor the characteristics of AlGaN/GaN heterojunctions and improve device stability for possible device applications in harsh environments in the future.

Acknowledgements This work was supported by National Natural Science Foundation of China (Grant Nos. 52161145404, 61905236, 51961145110), Fundamental Research Funds for the Central Universities (Grant Nos. WK3500000009, WK2100230020), Students' Innovation and Entrepreneurship Foundation of USTC (Grant No. CY2022X04), and partially carried out at the USTC Center for Micro and Nanoscale Research and Fabrication.

References

1 Zhang H, Huang C, Song K, et al. Compositionally graded III-nitride alloys: building blocks for efficient ultraviolet optoelectronics and power electronics. Rep Prog Phys, 2021, 84: 044401

2 Huang C, Zhang H, Sun H. Ultraviolet optoelectronic devices based on AlGaN-SiC platform: towards monolithic photonics integration system. Nano Energy, 2020, 77: 105149

3 Zhong Y, Zhang J, Wu S, et al. A review on the GaN-on-Si power electronic devices. Fundamental Res, 2022, 2: 462–475

4 Sun Y, Zhang H, Yang L, et al. Correlation between electrical performance and gate width of GaN-based HEMTs. IEEE Electron Dev Lett, 2022, 43: 1199–1202

5 Zhang H, Sun Y, Song K, et al. Demonstration of AlGaN/GaN HEMTs on vicinal sapphire substrates with large misoriented angles. Appl Phys Lett, 2021, 119: 072104

6 Zhang H, Liang F, Song K, et al. Demonstration of AlGaN/GaN-based ultraviolet phototransistor with a record high responsivity over 3.6×10^7 A/W. Appl Phys Lett, 2021, 118: 242105

7 Nela L, Ma J, Erine C, et al. Multi-channel nanowire devices for efficient power conversion. Nat Electron, 2021, 4: 284–290

8 Yang J Y, Yeom M J, Lee J, et al. Reconfigurable radio-frequency high-electron mobility transistors via ferroelectric-based gallium nitride heterostructure. Adv Elect Mater, 2022, 8: 2101406

9 Zhou F, Xu W, Ren F, et al. 1.2 kV/25 A normally off P-N junction/AlGaN/GaN HEMTs with nanosecond switching characteristics and robust overvoltage capability. IEEE Trans Power Electron, 2022, 37: 26–30

10 Nela L, Xiao M, Zhang Y, et al. A perspective on multi-channel technology for the next-generation of GaN power devices. Appl Phys Lett, 2022, 120: 190501

11 Cui P, Jia M, Chen H, et al. InAlN/GaN HEMT on Si with $f_{\max} = 270$ GHz. IEEE Trans Electron Dev, 2021, 68: 994–999

12 Yang L, Hou B, Jia F, et al. The DC performance and RF characteristics of GaN-based HEMTs improvement using graded AlGaN back barrier and Fe/C Co-doped buffer. IEEE Trans Electron Dev, 2022, 69: 4170–4174

13 Yu H, Parvais B, Peralagu U, et al. Back barrier trapping induced resistance dispersion in GaN HEMT: mechanism, modeling, and solutions. In: Proceedings of International Electron Devices Meeting (IEDM), 2022

14 Lee J H, Lisesivdin S B, Lee J H, et al. High figure-of-merit ($V_{\rm BR}^2/R_{\rm ON}$) AlGaN/GaN power HEMT with periodically C-doped GaN buffer and AlGaN back barrier. IEEE J Electron Dev Soc, 2018, 6: 1179–1186

15 He L, Li L, Zheng Y, et al. The influence of Al composition in AlGaN back barrier layer on leakage current and dynamic $R_{\rm ON}$ characteristics of AlGaN/GaN HEMTs. Phys Status Solidi A, 2017, 214: 1600824

16 Hamza K H, Nirmal D, Fletcher A S A, et al. Enhanced drain current and cut off frequency in AlGaN/GaN HEMT with BGaN back barrier. Mater Sci Eng-B, 2022, 284: 115863

17 Zhang Y, Guo R, Xu S, et al. High-performance high electron mobility transistors with GaN/InGaN composite channel and superlattice back barrier. Appl Phys Lett, 2019, 115: 072105

18 Kim J G, Kang S H, Janicki Ł, et al. Growth of AlGaN/GaN heterostructure with lattice-matched AlIn(Ga)N back barrier. Solid-State Electron, 2019, 152: 24–28

19 Malmros A, Gamarra P, Thorsell M, et al. Impact of channel thickness on the large-signal performance in InAlGaN/AlN/GaN HEMTs with an AlGaN back barrier. IEEE Trans Electron Dev, 2018, 66: 364–371

20 Han T, Zhao H, Han L, et al. Investigation into the carrier distribution and energy-band profile in AlGaN/GaN heterostructures with a graded AlGaN buffer. Semicond Sci Technol, 2018, 33: 115018

21 Hájek F, Hospodková A, Hubík P, et al. Transport properties of AlGaN/GaN HEMT structures with back barrier: impact of dislocation density and improved design. Semicond Sci Technol, 2021, 36: 075016

22 Liu X, Wang H Y, Chiu H C, et al. Analysis of the back-barrier effect in AlGaN/GaN high electron mobility transistor on free-standing GaN substrates. J Alloys Compd, 2020, 814: 152293

23 Zhang W, Li X, Zhang J, et al. Overcoming the poor crystal quality and DC characteristics of AlGaN/GaN/AlGaN double-heterostructure high electron mobility transistors. Phys Status Solidi A, 2016, 213: 2203–2207

24 Wang J, You H, Guo H, et al. Do all screw dislocations cause leakage in GaN-based devices? Appl Phys Lett, 2020, 116: 062104

25 Besendörfer S, Meissner E, Medjdoub F, et al. The impact of dislocations on AlGaN/GaN Schottky diodes and on gate failure of high electron mobility transistors. Sci Rep, 2020, 10: 17252

26 Divya P, Kumar A, Lee W H. Effects of SiNX passivation on GaN-HEMT DC characteristics. Mater Sci Semicond Process, 2022, 148: 106716

27 Lv Y, Lin Z, Corrigan T D, et al. Extraction of AlGaN/GaN heterostructure Schottky diode barrier heights from forward current-voltage characteristics. J Appl Phys, 2011, 109: 074512

28 Vertiatchikh A V, Eastman L F. Effect of the surface and barrier defects on the AlGaN/GaN HEMT low-frequency noise performance. IEEE Electron Dev Lett, 2003, 24: 535–537

29 Lu H, Yang L, Hou B, et al. AlN/GaN/InGaN coupling-channel HEMTs with steep subthreshold swing of sub-60 mV/decade. Appl Phys Lett, 2022, 120: 173502

30 Song W, Li Y, Zhang K, et al. Steep subthreshold swing in GaN negative capacitance field-effect transistors. IEEE Trans Electron Dev, 2019, 66: 4148–4150

31 Liu X, Gu H, Li K, et al. AlGaN/GaN high electron mobility transistors with a low sub-threshold swing on free-standing GaN wafer. AIP Adv, 2017, 7: 095305

32 Lu X, Ma J, Jiang H, et al. Low trap states in in situ SiN_x/AlN/GaN metal-insulator-semiconductor structures grown by metal-organic chemical vapor deposition. Appl Phys Lett, 2014, 105: 102911

33 Goswami A, Trew R J, Bilbro G L. Modeling of the gate leakage current in AlGaN/GaN HFETs. IEEE Trans Electron Dev, 2014, 61: 1014–1021

34 Mukherjee J, Chaubey R K, Rawal D S, et al. Analysis of the post-stress recovery of reverse leakage current in GaN HEMTs. Mater Sci Semicond Process, 2022, 137: 106222

35 Fang T, Wang R, Xing H, et al. Effect of optical phonon scattering on the performance of GaN transistors. IEEE Electron Dev Lett, 2012, 33: 709–711

36 Xu N, Hao R, Chen F, et al. Gate leakage mechanisms in normally off p-GaN/AlGaN/GaN high electron mobility transistors. Appl Phys Lett, 2018, 113: 152104

37 Chen Y H, Zhang K, Cao M Y, et al. Study of surface leakage current of AlGaN/GaN high electron mobility transistors. Appl Phys Lett, 2014, 104: 153509